Journal of Porphyrins and Phthalocyanines
J. Porphyrins Phthalocyanines 2025; **29**: 467–477
DOI: 10.1142/S1088424625500397

Published at https://www.worldscinet.com/jpp/

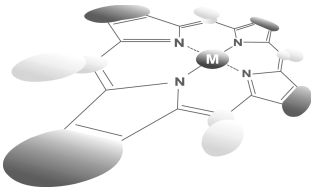

Si(IV) complexes of 10,20-diaryl-5,15-diazaporphyrin and 5,10,20-triaryl-5,15-diazaporphyrinoids: Evaluation of charge effect on the optical, redox, and magnetic properties

Kanta Sasaki[a], Yui Murata[b], Hiroya Suzuki[b], Mao Minoura[c], Rio Kitakado[d], Yoshifumi Kimura[d], Ko Furukawa[e], Haruyuki Nakano[f], and Yoshihiro Matano*[,a]

[a]*Department of Chemistry, Faculty of Science, Niigata University, Nishi-ku, Niigata 950-2181, Japan*
[b]*Department of Fundamental Sciences, Graduate School of Science and Technology, Niigata University, Nishi-ku, Niigata 950-2181, Japan*
[c]*Department of Chemistry, College of Science, Rikkyo University, Toshima-ku, Tokyo 171-8501, Japan*
[d]*Department of Applied Chemistry, Graduate School of Science and Engineering, Doshisha University, Kyotanabe, 610-0321, Japan*
[e]*Center for Coordination of Research Facilities, Institute for Research Administration, Niigata University, Nishi-ku, Niigata 950-2181, Japan*
[f]*Department of Chemistry, Graduate School of Science, Kyushu University, Nishi-ku, Fukuoka 819-0395, Japan*

Received 21 January 2025
Accepted 19 February 2025

Dedicated to Prof. Karl M. Kadish on the occasion of his 80th birthday

ABSTRACT: The central metals in group 14 metalloporphyrins significantly influence the optical, redox, and magnetic properties of the porphyrin π-electron systems. This study reports the first examples of Si(IV) complexes of 10,20-diaryl-5,15-diazaporphyrin (Ar_2DAP) and 5,10,20-triaryl-5,15-diazaporphyrin (Ar_3DAP), designed to explore the effects of *meso*-nitrogen atoms and net charge on these fundamental properties of the porphyrin ring. Reacting the free base of Ar_2DAP with $HSiCl_3$, followed by metathesis of axial ligands, yielded the corresponding Si(IV) complexes ($Ar_2DAPSiX_2$; X = OH, F). Copper-catalyzed *N*-phenylation of $Ar_2DAPSiF_2$ and subsequent redox reactions produced 18π- and 19π-electron derivatives of $Ar_3DAPSiF_2$. Nuclear magnetic resonance spectroscopy, cyclic voltammetry, and density functional theory calculations revealed that the diatropic ring-current effects derived from the aromatic 18π-electron systems of $Ar_2DAPSiX_2$ and $Ar_3DAPSiF_2$ strongly depend on the net charge and dipole moment of the DAP ligand. All Si(IV) complexes exhibited fluorescence, with Stokes shifts of 120–310 cm^{-1}. Measurements of fluorescence quantum yields and lifetimes indicated that *N*-phenylation primarily reduced the nonradiative decay rate constant. These findings provided insights into the influence of net charge on the aromatic character, as well as the optical and redox properties, of six-coordinate Si(IV) complexes of DAP derivatives.

KEYWORDS: diazaporphyrin, silicon complex, fluorescence, radical

*Correspondence to: Yoshihiro Matano, Department of Chemistry, Faculty of Science, Niigata University, Nishi-ku, Niigata 950-2181, Japan; Tel: +81-25-262-7734; Fax: +81-25-262-7734; E-mail: matano@chem.sc.niigata-u.ac.jp

INTRODUCTION

The central metals in group 14 metalloporphyrins play a crucial role in determining the optical, redox, and magnetic properties of porphyrin π-electron systems, as these properties are closely linked to the electronegativity, oxidation number, and axial ligands of the metal. Additionally, the chemical shifts of nuclear magnetic resonance (NMR)-active isotopes, such as ^{29}Si and ^{119}Sn, with a nuclear spin quantum number of ½, are often used as indices to evaluate the magnitude of ring currents induced by porphyrin ligands. Silicon(IV) porphyrin (Si porphyrin) complexes generally feature a hypervalent, six-coordinate Si center with two axial ligands. Their structure–property relationships and reactivities have been studied extensively [1–7]. For instance, Lemke *et al*. investigated a series of Si porphyrins with various axial ligands and peripheral substituents, revealing their crystal structures, optical and redox properties, and reactivities [3]. Multinuclear (^{29}Si and ^{19}F) NMR spectroscopy demonstrated the effects of the diamagnetic ring currents originating from the porphyrin ligand and the through-bond electronic influence of axial fluorine atoms on the metal center and porphyrin ligand. Similarly, Adler *et al*. observed that the identity of axially substituted silyloxy groups affects the planarity of the porphyrin ring in the solid state and influences the redox potentials [6]. Vaid *et al*. developed a unique approach leveraging group 14 elements, including Si, to stabilize the 20π-electron porphyrins (isophlorins) [7]. They synthesized a Si(IV) isophlorin complex via the 2e$^-$-reduction of Si(IV) complex of the 18π-electron aromatic 5,10,15,20-tetraphenylporphyrin (TPP) with sodium metal in tetrahydrofuran (THF). They observed that the highly ruffled isophlorin ligand exhibited strong paramagnetic ring-current effects in the ^{1}H and ^{29}Si NMR spectra. While these studies elucidated the structure–property relationships and reactivities of neutral Si porphyrins and related macrocycles, limited experimental data exist on the correlation between net charge and the fundamental properties of Si(IV) porphyrin complexes due to the scarcity of accessible ionic 18π-electron systems.

We have synthesized redox-switchable 5,10,15,20-tetraaryl-5,15-diazaporphyrin (Ar_4DAP) [8] and 5,10,20-triaryl-5,15-diazaporphyrin (Ar_3DAP) [9] as new families of 5,15-diazaporphyrin (DAP) to examine the effects of *meso*-nitrogen atoms and net charge on the optical and redox properties and reactivities of the porphyrin ring. Notably, the number of *meso-N*-substituents alters the net charge of the isoelectronic DAP ring. For example, in the same 18π-electron state, 10,20-diaryl-5,15-diazaporphyrin (Ar_2DAP) is neutral, Ar_3DAP is cationic (+1), and Ar_4DAP is dicationic (+2). Recently, we established a convenient method of synthesizing free bases of Ar_4DAP and reported the first difluorosilicon(IV) complexes of Ar_4DAP ($Ar_4DAPSiF_2$) **P1**, obtained as dication (18π), radical cation (19π), and neutral (20π) species (Scheme 1) [10]. Importantly, the electron-withdrawing Si(IV) center stabilized the neutral 20π-electron DAP ligand in **P1** while maintaining planarity. The ^{1}H, ^{29}Si, and ^{19}F NMR chemical shifts of the closed-shell derivatives of **P1** indicated weaker aromaticity compared to the isoelectronic porphyin ring in the difluorosilicon(IV) complex of TPP [3d]. Herein, we report novel six-coordinate Si(IV) complexes of Ar_2DAP ($Ar_2DAPSiX_2$; X = OH, F) and Ar_3DAP ($Ar_3DAPSiF_2$) to elucidate the effects of axial ligands and net charge on the optical and redox properties, as well as on diatropic ring-current effects derived from closed-shell 18π-electron systems. Additionally, the neutral 19π-electron $Ar_3DAPSiF_2$ radical was isolated and characterized.

RESULTS AND DISCUSSION

Scheme 2 illustrates the synthesis of new Si(IV) complexes of DAP derivatives. Treatment of the free base of 10,20-dimesityl-5,15-diazaporphyrin (mesityl = 2,4,6-trimethylphenyl) **1** [11] with excess trichlorosilane in the presence of triethylamine in CH_2Cl_2 for 24 h at room temperature, followed by stirring with an aqueous NaOH solution, afforded the dihydroxysilicon(IV) complex ($Ar_2DAPSi(OH)_2$) **2** as a reddish-purple solid in 47% yield after alumina column chromatography. The metathesis reaction of **2** with SbF_3 in CH_2Cl_2 was complete after 24 h at room temperature, yielding the difluorosilicon(IV) complex ($Ar_2DAPSiF_2$) **3** as a reddish-purple solid in 89% yield after recrystallization from CH_2Cl_2–hexane. Heating a mixture of **3**, diphenyliodonium hexafluorophosphate, and a catalytic amount of copper(II) benzoate in chlorobenzene for 2 h at 130 °C, followed by treatment with aqueous KPF_6 solution at room temperature,

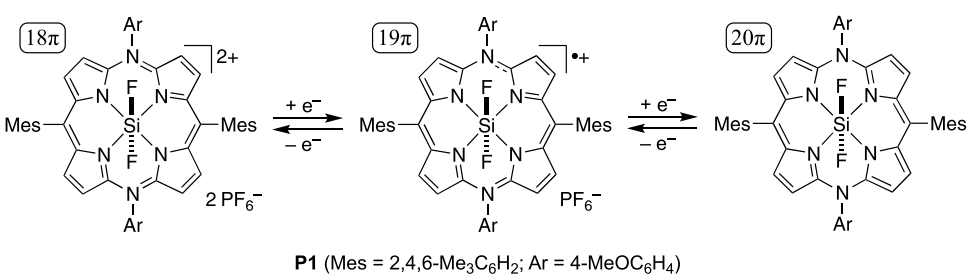

Scheme 1. Previously reported $Ar_4DAPSiF_2$ derivatives **P1**.

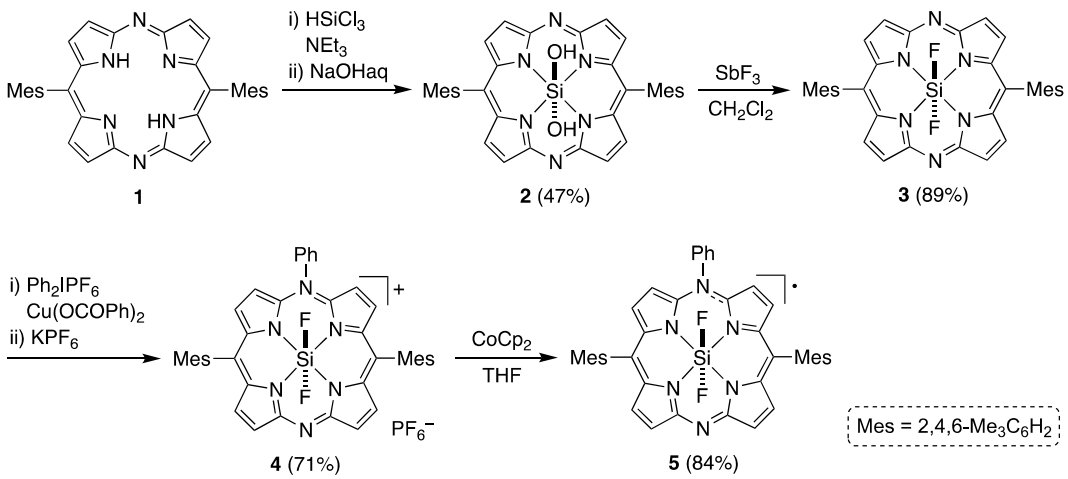

Scheme 2. Synthesis of Si(IV) complexes of DAP derivatives **2**–**5**.

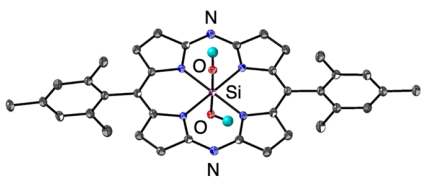

Δd_{RMS} = 0.033 Å (for DAP ring)

Bond lengths (Å)	
Si–N	1.9392(13)–1.9530(13)
Si–O	1.6873(11)–1.7159(11)
N_{meso}–C_{α}	1.3261(19)–1.3289(19)
C_{meso}–C_{α}	1.390(2)–1.397(2)

(a)

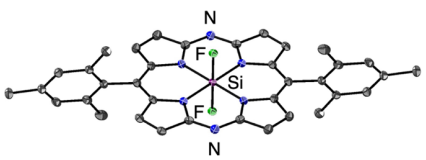

Δd_{RMS} = 0.015 Å (for DAP ring)

Bond lengths (Å)	
Si–N	1.9228(10)–1.9300(10)
Si–F	1.6507(7)
N_{meso}–C_{α}	1.3197(16)–1.3234(16)
C_{meso}–C_{α}	1.3891(17)–1.3916(17)

(b)

Fig. 1. ORTEP diagrams (50% probability ellipsoids), selected bond lengths, and root-mean-square deviations (Δd_{RMS}) of (a) **2** and (b) **3**. Hydrogen atoms are omitted for clarity except for the hydroxy groups of **2**.

afforded the difluorosilicon(IV) complex of 10,20-dimesityl-5-phenyl-5,15-diazaporphyrinium hexafluorophosphate ([$Ar_3DAPSiF_2$][PF_6]) **4** as a dark green solid in 71% yield after silica-gel column chromatography. Single-electron reduction of the 18π-electron cationic DAP ring in **4** with cobaltocene ($CoCp_2$) in THF quantitatively furnished the corresponding 19π-electron neutral radical ($Ar_3DAPSiF_2$) **5**, isolated as a dark greenish-yellow solid in 84% yield.

The new compounds were characterized by NMR and infrared (IR) spectroscopy, along with high-resolution electrospray ionization mass spectrometry (ESIMS). Positive-mode ESIMS profiles showed intense peaks corresponding to $[M+Na]^+$ (for **2** and **3**), $[M-PF_6]^+$ (for **4**), and $[M]^+$ (for **5**), while negative-mode profiles displayed peaks corresponding to $[M]^-$ (for **2** and **3**) and $[PF_6]^-$ (for **4**). The IR spectra of **2** and **4** revealed O–H and P–F stretching bands at ν_{max} values of 3501 and 832 cm^{-1}, respectively.

The structures of **2** and **3** were unambiguously confirmed by X-ray crystallography. Figure 1 presents the crystal structures and selected bond lengths, and Fig. S1 and Table S1 (in the Supporting Information) summarize supplementary details. In both compounds, the Si(IV) centers exhibit octahedral geometry, with oxygen or fluorine atoms occupying axial positions. The *meso*-mesityl groups are significantly twisted from the DAP ring (dihedral angles = 89.0–89.6° for **2** and 72.6° for **3**), suggesting negligible π-conjugation between them. The Si–N bond lengths in **3** [1.9228(10)–1.9300(10) Å] are slightly shorter than those in **2** [1.9392(13)–1.9530(13) Å], reflecting differences in electron density at the silicon center; replacing the axial ligands with more electronegative F atoms can relatively reduce the electron density of the silicon center. Similarly, the N_{meso}–C_{α} bond lengths in **2** [1.3261(19)–1.3289(19) Å] are slightly longer than those in **3** [1.3197(16)–1.3234(16) Å], suggesting elongation of Si–N bonds induces elongation of N_{meso}–C_{α} bonds.

The Si–N and Si–F bond lengths in **3** [Si–F: 1.6507(7) Å] are comparable to those observed in isoelectronic difluorosilicon(IV) complexes of 5,10,15,20-tetraarylporphyrins [aryl=*p*-MeC_6H_4 *p*-$CF_3C_6H_4$; Si–N: 1.911(2)–1.925(2) Å, Si–F: 1.628(2)–1.652(2) Å] [3c]. The Si–F bond length in **3** is much closer to that in a six-coordinate, octahedral SiF_6^{2-} (1.706 Å) [12, 13] than that in four-coordinate, tetrahedral SiF_4 (1.5598 Å) [13, 14], supporting the hypervalent nature of the Si(IV) centers in $Ar_2DAPSiX_2$. Both compounds exhibit highly planar DAP rings, with root-mean-square deviations (Δd_{RMS}) of 0.015–0.033 Å. The average values of the harmonic oscillator model of aromaticity (HOMA) [15], determined from the 18 C–X (X=C, N) bonds making up the 18π-electron network, for **2** (0.752) and **3** (0.741) indicate aromatic character comparable to previously reported nickel(II), palladium(II), and platinum(II) complexes of 18π-electron Ar_2DAP with the same *meso*-mesityl groups (M=Ni, HOMA=0.734; M=Pd, HOMA=0.753; M=Pt, HOMA=0.735) [11, 16].

The ^{1}H NMR spectra of **2**, **3**, and **4** are shown in Fig. 2. The pyrrolic-β proton signals for **2** and **3** in $CDCl_3$ appeared as two doublets (each, 4H) at 9.37/8.99 and 9.44/9.07 ppm, respectively, while those for **4** in CD_2Cl_2 appeared as four doublets (each, 2H) at 9.55/9.06/9.05/8.57 ppm. These downfield-shifted ^{1}H signals reflect significant diatropic ring currents derived from the 18π-electron DAP rings. The ^{29}Si{^{1}H} NMR signals for **2**, **3**, and **4** were observed at −205.7, −209.4 (t, $J_{Si\text{-}F}$=199 Hz), and −207.5 ppm (t, $J_{Si\text{-}F}$=204 Hz), respectively, whereas the ^{19}F{^{1}H} NMR signals for **3** and **4** were observed at −119.1 and −117.3 ppm (vs. $CFCl_3$), respectively. The upfield-shifted ^{29}Si and ^{19}F signals reflected the aromatic nature of the DAP π-electron systems. Notably, the ^{29}Si and ^{19}F chemical shifts of the neutral $Ar_2DAPSiF_2$ **3** and the cationic $Ar_3DAPSiF_2$ **4** differed significantly. The ^{29}Si and ^{19}F resonances of **4** shifted slightly downfield relative to the corresponding resonances of **3**, attributed to two main factors affecting the magnetic shielding and deshielding of these resonances. One factor is the inductive effect from the DAP ligands through the Si–N and Si–F bonds, and the other is the diatropic ring-current effect due to the DAP 18π-electron system. Thus, the decrease in both the electron density of the Si and F atoms and ring-current density of the DAP π-ligand weakens the shielding effects on these nuclei, resulting in the downfield shifts of the corresponding signals (vide infra).

To further understand the ring-current effects of DAP ligands, density functional theory (DFT) calculations were conducted on model compounds **3m** and **4m** (with *meso*-mesityl groups replaced by phenyl groups). Figure 3a shows the frontier orbitals and energies of the optimized structures. Compared to **3m**, both the highest occupied molecular orbital (HOMO) and the lowest unoccupied molecular orbital (LUMO) of **4m** are significantly stabilized, reflecting the positive charge of the DAP ring in **4m**. The LUMO energy is more affected by the *N*-phenyl group than the HOMO because the LUMO has a large MO coefficient on the *meso*-nitrogen atom, resulting in a narrow HOMO–LUMO gap ($\Delta E_{H\text{–}L}$=2.37 eV for **4m** vs. 2.65 eV for **3m**). Thus, the *N*-phenyl substituent has

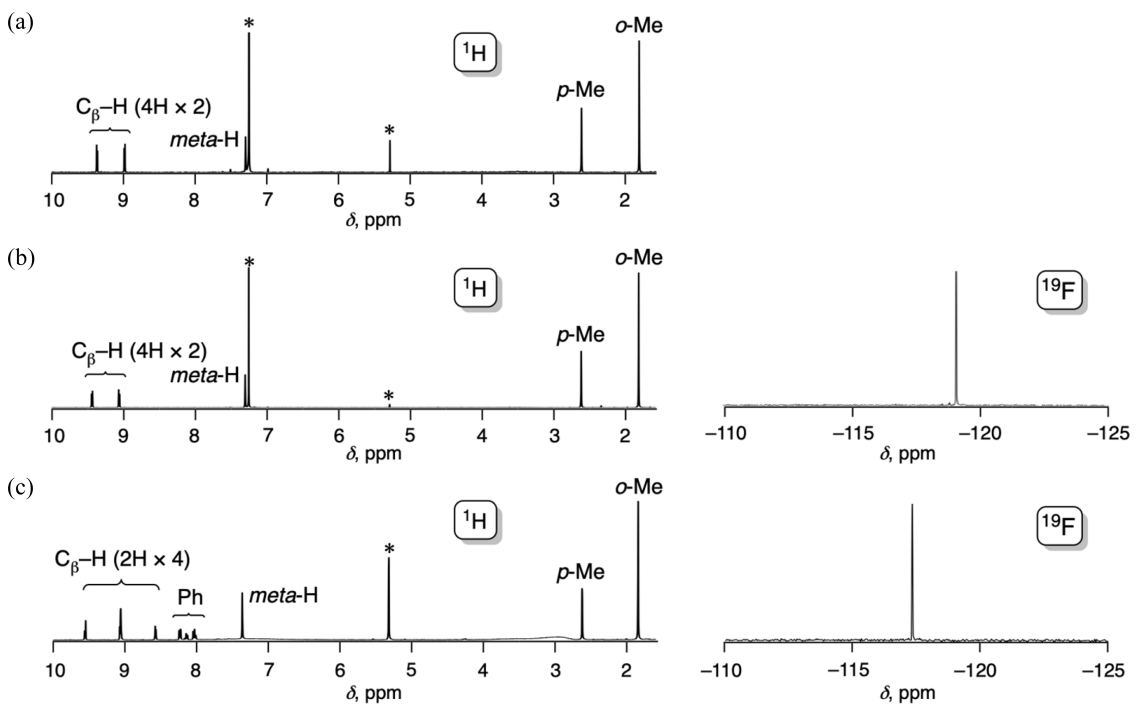

Fig. 2. ^{1}H NMR (400 MHz; 10–1.5 ppm) and ^{19}F{^{1}H} NMR (376 MHz; −110 – −125 ppm) spectra of (a) **2** in $CDCl_3$, (b) **3** in $CDCl_3$, and (c) **4** in CD_2Cl_2. Asterisks indicate the residual solvent peaks.

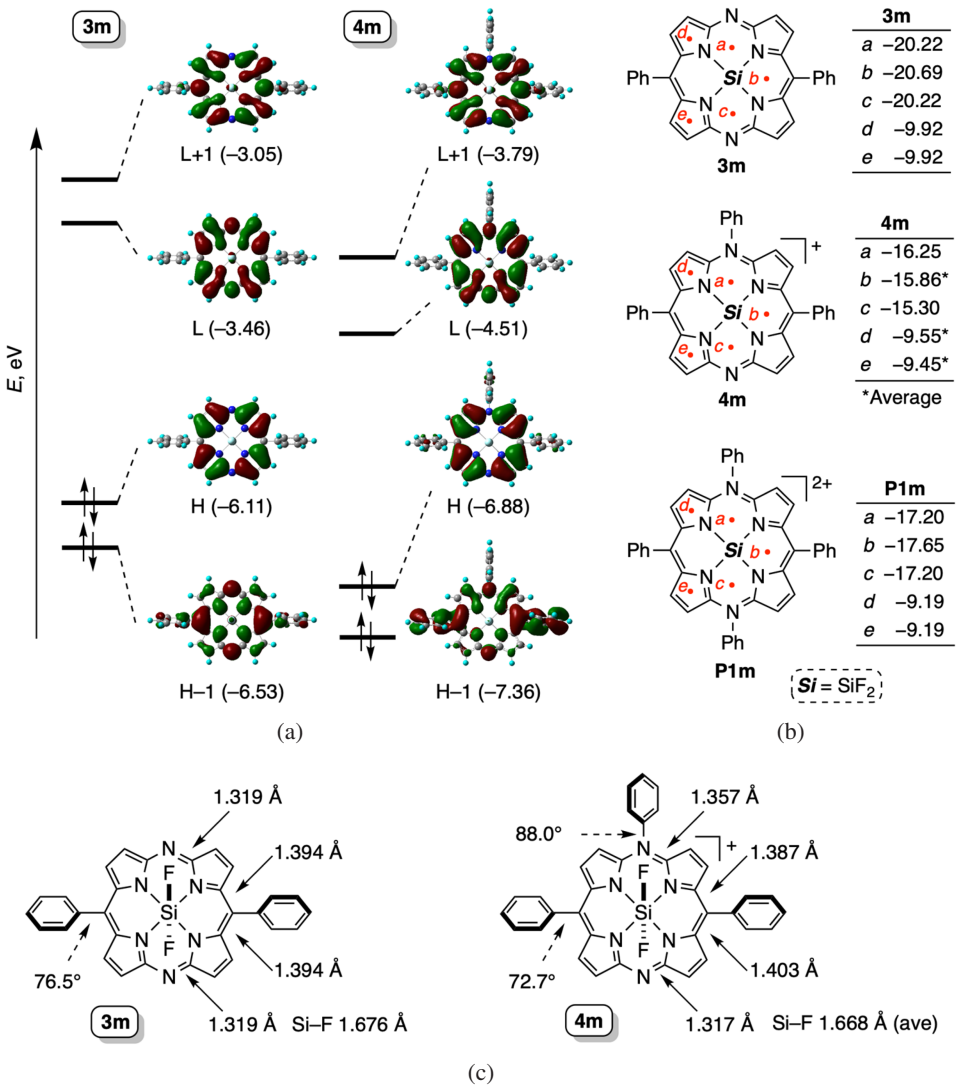

Fig. 3. (a) Selected Kohn-Sham orbitals and their energies (in eV) of **3m** and **4m** calculated by the DFT method. H = HOMO, L = LUMO. (b) NICS(0) values (in ppm) calculated for **3m**, **4m**, and **P1m** (18π dication) at positions *a*–*e*. (c) Selected bond lengths and torsion angles of **3m** and **4m**.

a substantial amount of the positive charge and acts as an electron-withdrawing group (Fig. S2). Nuclear independent chemical shifts (NICSs) [17] were calculated at multiple positions in the π-planes and compared for **3m**, **4m**, and **P1m** [10]. As shown in Fig. 3b, **3m** exhibits more negative NICS(0) values at positions *a*, *b*, and *c* (−20.22, −20.69, and −20.22 ppm) than **4m** (−16.25, −15.86, and −15.30 ppm) and **P1m** (−17.20, −17.65, and −17.20 ppm, respectively), indicating a stronger macrocyclic diatropic ring-current effect in **3m**. These differences are attributed to variations in ring-current density, with the neutral DAP ring in **3m** generating a larger density than the positively charged DAP rings in **4m** and **P1m**. The calculated dipole moment of **4m** (7.34 D) suggests that its polarized structure localizes π-electron density on the *meso*-nitrogen at position 15, weakening the diatropic ring-current effects compared to **P1m**. The ^{19}F chemical shifts of the three models, calculated at the DFT level with gauge-including atomic orbital, shifted upfield in the order **3m** (–169.5 ppm), **4m** (–166.0 ppm), **P1m** (–162.8 ppm), supporting the trend observed for **3**, **4**, and **P1** [18]. The ^{19}F chemical shifts followed the same trend as the Mulliken charges of F atoms (–0.482 for **3m**, –0.470 for **4m**, –0.459 for **P1m**; see Table S1) in contrast to the trend of the NICS(0) values, which shifted positively in the order **3m** < **P1m** < **4m** (vide supra). This highlighted the dominance of inductive effect over ring-current effect on the ^{19}F chemical shift. These findings emphasize how net charge influences the ring-current effects in DAP 18π-electron systems.

The redox properties of **2**, **3**, and **4** in CH_2Cl_2 were analyzed using cyclic voltammetry (CV) with Bu_4NPF_6 as the supporting electrolyte. As shown in Fig. 4, $Ar_2DAPSi(OH)_2$ **2** and $Ar_2DAPSiF_2$ **3** exhibited three reversible redox processes at $E_{1/2}$ = −1.72, −1.20, and +1.03 V for **2**, and $E_{1/2}$ = −1.70, −1.10, and +1.08 V for **3**

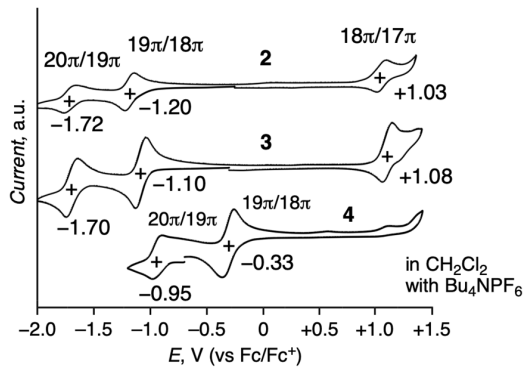

Fig. 4. Cyclic voltammograms of **2**, **3**, and **4** in CH_2Cl_2 with Bu_4NPF_6 as the supporting electrolyte. Scan rate = 60 mV s^{-1}. Half-wave potentials ($E_{1/2}$) vs. Fc/Fc^+ are indicated.

(vs. the ferrocene/ferrocenium couple; Fc/Fc^+). The $E_{1/2}$ values of **3** were positively shifted compared to those of **2**, likely due to the electron-withdrawing nature of axial fluorine ligands in **3**. In contrast, $[Ar_3DAPSiF_2][PF_6]$ **4** displayed two reversible DAP-centered redox couples at $E_{1/2}$ = −0.95 (20π/19π) and −0.33 V (19π/18π), significantly shifted to the positive side (by 0.76–0.79 V) compared to **3**, reflecting the stabilization of DAP frontier orbitals induced by *N*-phenylation.

The ultraviolet/visible/near infrared (UV/vis/NIR) absorption and emission spectra of **2**, **3**, **4**, and **5** in CH_2Cl_2 are shown in Fig. 5 and the corresponding optical data are summarized in Table 1. The Soret and Q bands, with absorption maxima (λ_{abs}) of 396/386 and 579/579 nm, respectively, were observed in the absorption spectra of $Ar_2DAPSiX_2$ **2/3**, while the corresponding absorption bands of the 18π-electron $[Ar_3DAPSiF_2][PF_6]$ **4** were observed at longer wavelengths (λ_{abs} = 392 and 621 nm, respectively). The absorption bands of **3** and **4** were assigned from the time-dependent DFT (TD-DFT) calculations for the model compounds, **3m** and **4m**, respectively, which revealed that the lowest excited states were primarily comprised of the HOMO-to-LUMO π–π* transitions of the corresponding DAP chromophores (Table 2). Compounds **2** and **3** emitted fluorescence with maxima (λ_{em}) of 586 and 583 nm, respectively, whereas **4** emitted red-shifted fluorescence with λ_{em} of 633 nm. From the absorption and fluorescence spectra, the optical HOMO–LUMO gaps of **2**, **3**, and **4** were determined to be 2.13, 2.13, and 1.98 eV, respectively. As supported by the DFT calculations for the models (Fig. 3), adding a positive charge to the 18π-electron system greatly stabilized the LUMO relative to the HOMO, resulting in a decrease in the HOMO–LUMO gap. The Stokes shifts increased in the order: **3** (120 cm^{-1}) < **2** (260 cm^{-1}) < **4** (310 cm^{-1}), reflecting slight differences in the reorganization energies of the molecules in the excited states. The UV/vis/NIR absorption spectrum of the 19π-electron $Ar_3DAPSiF_2$ radical **5** exhibited an intense NIR absorption band (λ_{abs} = 782 nm) originating from the

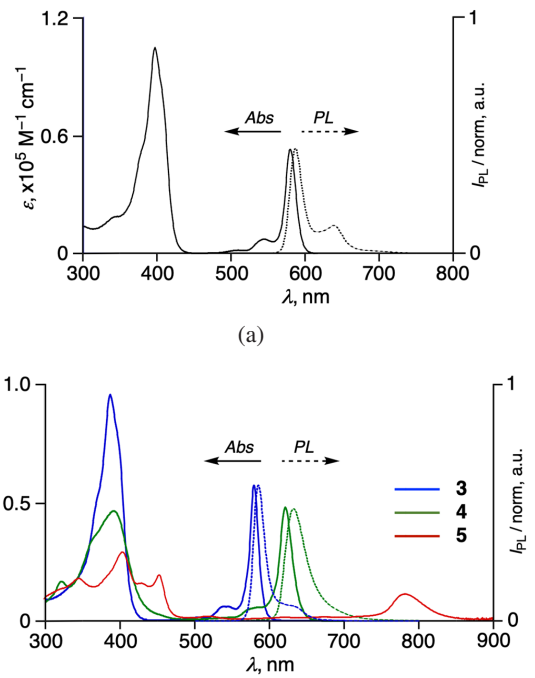

Fig. 5. UV/vis/NIR absorption (solid line) and emission (dotted line) spectra of (a) **2** and (b) **3**, **4**, and **5** in CH_2Cl_2.

Table 1. Optical and photophysical data for **2**, **3**, **4**, and **5**.

DAP	λ_{abs} [nm] (logε)[b]	λ_{em} [nm][c] (Φ_{em}[d]; τ_f [ns][e])	k_r [s^{-1}][f]	k_{nr} [s^{-1}][g]
2	396 (4.02), 579 (4.72)	586 (0.050; 1.46)	3.4×10^7	6.5×10^8
3	386 (4.98), 579 (4.76)	583 (0.050; 1.01)	5.0×10^7	9.4×10^8
4	392 (4.67), 621 (4.68)	633 (0.127; 2.48)	5.1×10^7	3.5×10^8
5	406 (4.47), 782 (4.08)	N.m.	N.d.	N.d.

[a]Measured in CH_2Cl_2. N.m. = Not measured. N.d. = Not determined. [b]Absorption maxima and logarithms of molecular extinction coefficients (in parentheses). [c]Emission maxima: λ_{ex} = 395 nm (for **2**), 390 nm (for **3** and **4**). [d]Absolute emission quantum yields: λ_{ex} = 395 nm (for **2**), 390 nm (for **3** and **4**). [e]Fluorescence lifetimes: λ_{ex} = 400 nm (for **2**, **3**, and **4**). [f]Radiative decay rate constants. [g]Non-radiative decay rate constants.

Table 2. Excitation energies and oscillator strengths of **3m**, **4m**, and **5m** calculated by the TD-DFT method.[a]

State	Excitation energy [eV/nm] (Oscillator strength)	Excitation (Weight [%])
3m		
1	2.35/527 (0.206)	HOMO => LUMO (80.9), HOMO−1 => LUMO+1 (18.7)
3	3.22/385 (0.500)	HOMO−1 => LUMO (35.5), HOMO−1 => LUMO+1 (33.6)
5	3.32/373 (1.332)	HOMO−1 => LUMO+1 (68.7), HOMO => LUMO (16.4)
9	3.43/361 (0.268)	HOMO−5 => LUMO (67.8)
15	3.76/330 (0.164)	HOMO−5 => LUMO+1 (87.0)
17	3.77/329 (0.367)	HOMO−9 => LUMO (69.5)
4m		
1	2.18/569 (0.337)	HOMO => LUMO (90.7)
11	3.16/393 (0.502)	HOMO−1 => LUMO+1 (65.3)
13	3.22/386 (0.357)	HOMO−4 => LUMO+1 (25.4), HOMO => LUMO+1 (22.1)
18	3.48/356 (0.857)	HOMO−11 => LUMO (29.9), HOMO => LUMO+1 (17.2)
19	3.68/337 (0.445)	HOMO−5 => LUMO+1 (66.9), HOMO−9 => LUMO+1 (18.8)
5m		
2	1.76/703 (0.177)	HOMO(β) => SOMO(β) (92.1)
10	3.10/399 (0.104)	HOMO−9(β)=> SOMO(β) (47.0)
11	3.13/396 (0.469)	HOMO(α) => LUMO(α) (14.2), HOMO(β) => LUMO(β) (13.5)
20	3.36/369 (0.340)	HOMO−9(β) => SOMO(β) (45.6)
21	3.38/366 (0.461)	HOMO−1(α) => LUMO(α) (43.7), HOMO−1(β) => LUMO(β) (20.4)

[a]B3LYP/6-311G(d,p) (PCM, CH_2Cl_2) at the optimized structures. The states whose oscillator strengths are less than 0.1 are not included.

HOMO(β)-to-SOMO(β) transition, where SOMO stands for singly occupied molecular orbital. This absorption band was blue-shifted compared with a similar NIR absorption band observed for the isoelectronic Ar_4DAP-SiF_2 cation radical **P1** (λ_{abs} = 865 nm).

To reveal the excited-state dynamics of the present Ar_nDAP derivatives, the fluorescence quantum yields (Φ_f) and lifetimes (τ_f) of **2**, **3**, and **4** in CH_2Cl_2 were measured. The radiative and nonradiative rate constants (k_r and k_{nr}) obtained from the τ_f and Φ_f values are summarized in Table 1. Single-exponential decay profiles were observed for **2** and **3**, with τ_f of 1.46 and 1.01 ns, respectively, when excited at the Soret band (λ_{ex} = 400 nm). The k_r and k_{nr} values of **3** are larger than the corresponding values of **2**, although the reason is not clear. A single-exponential decay profile was also observed for **4**, revealing that the cationic DAP ring in **4** existed as a single emissive component in solution.

Figure 6a shows the electron paramagnetic resonance (EPR) spectrum of a CH_2Cl_2 solution of **5** at room temperature. The neutral 19π-electron radical **5** exhibited an EPR signal at g = 2.0023, close to the g value observed

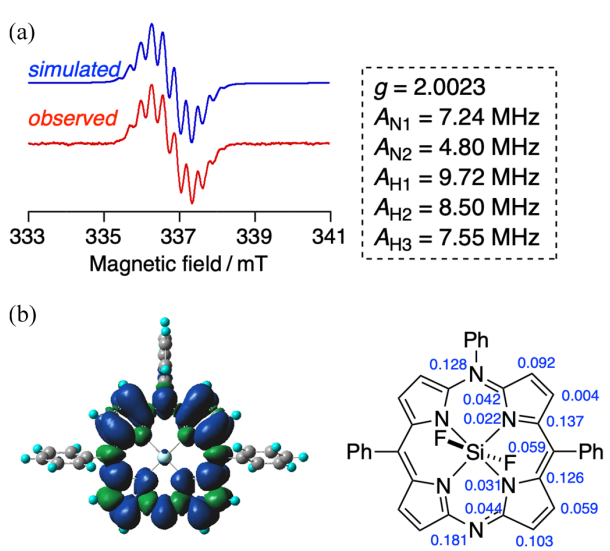

Fig. 6. (a) EPR spectrum of **5** in CH_2Cl_2 observed at room temperature. (b) Spin density distribution at the optimized structure (left) and spin densities at the DAP ring (right) of **5m** calculated by the DFT method.

for the isoelectronic $Ar_4DAPSiF_2$ cation radical **P1** (g=2.00195). Hyperfine coupling was observed for **5** and was well simulated by the DFT calculations for the model, **5m**, revealing that the unshared electron spin was fully delocalized over the DAP ring (Fig. 6b). The high air-stability of **5** in the solid state was attributed to this efficient delocalization of the electron spin over the DAP ring.

In summary, the first examples of Si(IV) complexes of Ar_2DAP were synthesized via the reaction of the corresponding free base with $HSiCl_3$ and subsequent metathesis of the axial ligands. Si(IV) complexes of the Ar_3DAP derivatives were also synthesized as both the 18π-electron cation and the 19π-electron neutral radical, using copper-catalyzed *N*-phenylation and subsequent redox reaction. The six-coordinate Si(IV) center and highly planar DAP ligand in $Ar_2DAPSiX_2$ (X=OH, F) were elucidated by X-ray crystallography. NMR spectroscopy and DFT calculations revealed that the diatropic ring-current effects decreased with an increase in the positive charge and dipole moment of the DAP ligands. Furthermore, UV/vis/NIR absorption and emission spectroscopy revealed that the positive charge introduced onto the 18π-electron DAP ring by *N*-phenylation induced red-shifts in the absorption and emission maxima of the $Ar_nDAPSiF_2$ chromophores. CV supported the stronger stabilizing effect of adding a positive charge on the LUMO level compared to the HOMO level, resulting in a decrease in the HOMO–LUMO gap of the 18π-electron DAP ligand. The 19π-electron neutral radical of $Ar_3DAPSiF_2$ was found to be air-stable in the solid state due to the efficient delocalization of the unshared electron spin. The series of Si(IV) complexes of Ar_nDAP (n=2, 3, and 4) synthesized in this study provides a promising platform for obtaining valuable information about the effects of net charge on the optical, redox, and magnetic properties of the porphyrin 18π-electron system.

EXPERIMENTAL

General

All melting points were recorded on a Yazawa micro melting point apparatus (BY-1) and are uncorrected. The ^{1}H NMR, ^{13}C{^{1}H} NMR, ^{19}F{^{1}H} NMR, and ^{29}Si{^{1}H} NMR spectra were recorded on a Bruker 400 MHz spectrometer using $CDCl_3$ or CD_2Cl_2 as a solvent. Chemical shifts are reported as relative values vs tetramethylsilane (0 ppm in $CDCl_3$) or a residual solvent peak (5.32 ppm in CD_2Cl_2). High-resolution mass spectra (HRMS) were measured on a Thermo Fisher Scientific EXACTIVE Plus Fourier-transform orbitrap mass spectrometer (ESI). IR (Attenuated Total Reflection; ATR) spectra were obtained on a JASCO FT/IR4600 spectrometer. UV/vis/NIR absorption and emission spectra were measured at room temperature on JASCO V-530 and EP-8300 spectrometers, respectively. Absolute fluorescence quantum yields were measured on a Hamamatsu Photonics Quantaurus-QY spectrometer. Thin-layer chromatography was performed with Alt. 5554 DC-Alufolien Kieselgel 60 F254 (Merck), and preparative column chromatography was performed using Silica Gel 60 spherical, neutrality (Nacalai tesque). All reactions were performed under an argon atmosphere. Compound **1** was prepared according to the literature method [11]. Other chemicals and solvents were of reagent grade quality and used without further purification unless otherwise noted. The synthetic procedures and characterization data of new compounds are described below. The IR, mass, and ^{1}H NMR spectra are shown in the Supporting Information.

Synthesis and characterization

Synthesis of 2

To a well dried Schlenk tube containing **1** (99.5 mg, 0.181 mmol) was added CH_2Cl_2 (20 mL), Et_3N (800 μL, 5.74 mmol), and $HSiCl_3$ (400 μL, 4.08 mmol), and the mixture was stirred at room temperature under Ar atmosphere. After 24 h, the reaction mixture was quenched with 1 M NaOHaq at 0 °C, and the separated organic phase was washed with brine, dried over Na_2SO_4, and concentrated under reduced pressure to leave a solid residue, which was subjected to alumina column chromatography (CH_2Cl_2/acetone=20/1). The bright pink fraction (R_f=0.18; CH_2Cl_2/MeOH=20/1) was collected and evaporated to leave a solid, which was reprecipitated from CH_2Cl_2–hexane to afford **2** as a reddish purple crystalline solid (51.4 mg, 47%). Mp >300 °C. ^{1}H NMR ($CDCl_3$, 400 MHz): δ_H, ppm 9.37 (d, 4H, J=4.8 Hz, pyrrole-β), 8.99 (d, 4H, J=4.8 Hz, pyrrole-β), 7.31 (s, 4H, Mes-*meta*), 2.64 (s, 6H, *para*-Me), 1.83 (s, 12H, *ortho*-Me). ^{13}C{^{1}H} NMR ($CDCl_3$, 176 MHz): δ_C, ppm 152.5, 145.3, 139.2, 138.9, 134.6, 133.2, 132.8, 128.2, 120.1, 21.58, 21.46. ^{29}Si{^{1}H} NMR ($CDCl_3$, 139 MHz): δ_{Si}, ppm −205.7. HRMS (ESI) positive mode: m/z 631.2239 (calcd. for $C_{36}H_{32}N_6O_2Si$+Na: 631.2248, $[M+Na]^+$); negative mode: m/z 608.2359 (calcd. for $C_{36}H_{32}N_6O_2Si$: 608.2361, $[M]^-$). IR (ATR): ν, cm^{-1} 3501 (OH).

Synthesis of 3

To a poly(tetrafluoroethylene) vessel containing a CH_2Cl_2 solution (15 mL) of **2** (50.1 mg, 0.0823 mmol) was added SbF_3 (28.7 mg, 0.161 mmol) at room temperature. The mixture was stirred for 24 h at room temperature and then filtered through a Celite bed. The organic layer separated from the filtrate was washed with a saturated $NaHCO_3$aq and brine, dried over Na_2SO_4, and concentrated under reduced pressure to leave a solid residue, which was reprecipitated from CH_2Cl_2–hexane to afford **3** as a reddish

purple solid (44.9 mg, 89%). Mp > 300 °C. R_f = 0.89; (CH_2Cl_2/MeOH = 20/1). ^{1}H NMR ($CDCl_3$, 400 MHz): δ_H, ppm 9.44 (d, 4H, J = 4.8 Hz, pyrrole-β), 9.07 (d, 4H, J = 4.8 Hz, pyrrole-β), 7.31 (s, 4H, Mes-*meta*), 2.63 (s, 6H, *para*-Me), 1.83 (s, 12H, *ortho*-Me). ^{13}C{^{1}H} NMR ($CDCl_3$, 176 MHz): δ_C, ppm 152.9, 145.8, 139.3, 139.1, 134.2, 133.6, 133.1, 128.3, 120.2, 21.51, 21.47. ^{19}F{^{1}H} NMR ($CDCl_3$, 376 MHz): δ_F, ppm −119.1. ^{29}Si{^{1}H} NMR ($CDCl_3$, 139 MHz): δ_{Si}, ppm −209.4 (t, $J_{Si\text{-}F}$ = 199 Hz). HRMS (ESI) positive mode: *m/z* 635.2153 (calcd. for $C_{36}H_{30}F_2N_6Si$+Na: 635.2161, $[M+Na]^+$); negative mode: *m/z* 612.2267 (calcd. for $C_{36}H_{30}F_2N_6Si$: 612.2275, $[M]^-$).

Synthesis of 4

A mixture of **3** (41.0 mg, 0.0669 mmol), $Cu(OCOPh)_2$ (2.29 mg, 0.00749 mmol), Ph_2IPF_6 (86.8 mg, 0.204 mmol), and chlorobenzene (7 mL) was stirred for 2 h at 130 °C. After cooling to room temperature, $AgPF_6$ (3.85 mg, 0.0152 mmol) and an aqueous solution of KPF_6 were subsequently added, and the mixture was vigorously stirred. After the anion was completely exchanged (checked by TLC), the organic layer was separated, dried over Na_2SO_4, and concentrated under reduced pressure to leave a solid residue, which was subjected to silica-gel column chromatography (CH_2Cl_2/MeOH = 200/1). The dark green fraction (R_f = 0.25; CH_2Cl_2/MeOH = 20/1) was collected and evaporated to leave a solid, which was reprecipitated from CH_2Cl_2–cyclohexane to afford **4** as a dark green solid (39.7 mg, 71%). Mp > 300 °C. ^{1}H NMR (CD_2Cl_2, 400 MHz): δ_H, ppm 9.55 (d, 2H, J = 5.2 Hz, pyrrole-β), 9.06 (d, 2H, J = 5.2 Hz, pyrrole-β), 9.05 (d, 2H, J = 4.8 Hz, pyrrole-β), 8.57 (d, 2H, J = 5.2 Hz, pyrrole-β), 8.24-8.22 (m, 2H, Ph), 8.16-8.13 (m, 1H, Ph), 8.05-8.00 (m, 2H, Ph), 7.36 (s, 4H, Mes-*meta*), 2.62 (s, 6H, *para*-Me), 1.84 (s, 12H, *ortho*-Me). ^{13}C{^{1}H} NMR (CD_2Cl_2, 176 MHz): δ_C, ppm 154.7, 150.1, 147.2, 145.9, 140.8, 140.3, 138.7, 137.3, 137.0, 135.0, 133.0, 131.8, 130.2, 129.8, 129.1, 128.7, 126.3, 26.90, 21.2. ^{19}F{^{1}H} NMR (CD_2Cl_2, 376 MHz): δ_F, ppm −117.3. ^{29}Si{^{1}H} NMR (CD_2Cl_2, 139 MHz): δ_{Si}, ppm −207.5 (t, $J_{Si\text{-}F}$ = 204 Hz). ^{31}P{^{1}H} NMR (CD_2Cl_2, 162 MHz): δ_P, ppm −144.5 (sept, $J_{P\text{-}F}$ = 710 Hz). HRMS (ESI) positive mode: *m/z* 689.2652 (calcd. for $C_{42}H_{35}F_2N_6Si$: 689.2655, $[M-PF_6]^+$); negative mode: *m/z* 144.9646 (calcd. for PF_6: 144.9647, $[PF_6]^-$). IR (ATR): ν, cm^{-1} 832 (P–F).

Synthesis of 5

A mixture of **4** (20.4 mg, 0.0224 mmol), cobaltocene (9.63 mg, 0.0509 mmol), and THF (10 mL) was stirred for 5 min at room temperature. The reaction mixture was evaporated to leave a solid, which was reprecipitated from MeOH-CH_2Cl_2 to afford **5** as a dark yellow green solid (14.1 mg, 84%). Mp >300 °C. R_f = 0.89 (CH_2Cl_2/MeOH = 20/1). HRMS (ESI) positive mode: *m/z* 689.2649 (calcd. for $C_{42}H_{35}F_2N_6Si$: 689.2655, $[M]^+$).

X-ray crystallographic analysis

Single crystals of **2** and **3** were grown from chloroform–octane at room temperature. CCDC Deposition Numbers-2415645–2415646 contain the supplementary crystallographic data for these compounds. These data are provided free of charge by the joint Cambridge Crystallographic Data Centre and Fachinformationszentrum Karlsruhe. Selected structure parameters are as follows. **2**•H_2O: $C_{36}H_{34}N_6O_3Si$, MW = 626.78, 0.010×0.010×0.010 mm, monoclinic, $P2_1$/c, a = 13.894(5) Å, b = 27.056(9) Å, c = 7.986(3) Å, β = 97.895(7)°, V = 2973.6(17) Å^3, Z = 4, ρ_{calcd} = 1.400 g.cm^{-3}, μ = 0.47 cm^{-1}, collected 67338, independent 6832, parameters 431, R_w = 0.1306 (all data), R_1 = 0.0449 (I > 2.0σ(I)), GOF = 1.081. **3**: $C_{36}H_{30}F_2N_6Si$, MW = 612.75, 0.100×0.100×0.100 mm, monoclinic, $P2_1$/n, a = 7.9220(4) Å, b = 21.6343(12) Å, c = 9.1833(5) Å, β = 112.900(2)°, V = 1449.85(14) Å^3, Z = 2, ρ_{calcd} = 1.404 g.cm^{-3}, μ = 1.33 cm^{-1}, collected 34736, independent 3336, parameters 208, R_w = 0.0965 (all data), R_1 = 0.0359 (I > 2.0σ(I)), GOF = 1.080.

Computational details

The geometries of model compounds were optimized with the DFT method. The basis sets used for the optimization were 6-311G(d,p) basis set [19]. The functional of DFT was the Becke, three-parameter, Lee–Yang–Parr (B3LYP) exchange-correlation functional [20]. The optimized geometries were confirmed to be minima by vibrational analysis. We confirmed that the optimized geometries were not in a saddle but in stable points. The Cartesian coordinates and computed total energies of calculated models are summarized in Table S1 in the Supporting Information. The excitation energies and oscillator strengths listed in Table 2 were computed with the TD-DFT method. The solvent effect was incorporated in both the DFT and TD-DFT calculations using the polarizable continuum model (PCM) with the integral equation formalism variant [21]. The NICS [17] were calculated at the Hartree–Fock level with gauge-including atomic orbitals (GIAOs) at the DFT optimized geometries. The basis set used for the NICS calculations was 6-31+G(d) [19c, 22]. The solvent effect was not included in the NICS calculations. The ^{19}F chemical shifts were calculated at the DFT level with GIAOs, including solvent effect, at the DFT optimized geometries. The functional, basis sets, and solvent model used for the chemical shift calculations were the same as those used for the geometry optimization. All the calculations were carried out using the Gaussian 16 suite of programs [23].

Fluorescence lifetime measurements

The fluorescence lifetimes of **2**, **3** and **4** were measured using a streak camera as a fluorescence detector. The excitation pulse (400 nm) was generated by taking

the second harmonic pulse of the fundamental output of an amplified Ti:Sapphire laser system (Spectra Physics, Spitfire XPpro). Compounds **2**, **3**, and **4** showed single-exponential decay profiles with the lifetimes indicated in the text.

EPR measurements

The electron paramagnetic resonance (EPR) spectrum was measured at room temperature by using a JEOL JES-FA200 spectrometer equipped with an OXFORD ESR900 He-flow cryostat. A sample was prepared as a 0.1 mM solution in CH_2Cl_2. After three freeze-pump-thaw cycles, the solution sample in a quartz tube was sealed by a frame. Spectral simulation was performed using EasySpin [24], which is a MATLAB toolbox meant for this. The static magnetic field and microwave frequency were measured by an Echo Electronics EFM-2000 gauss meter and a TakedaRiken TR5212 microwave counter, respectively.

Acknowledgments

This work was supported by JSPS KAKENHI (23K23329 to YM, 21K04980 to HN) from MEXT, Japan. We thank Prof. Tomohiro Higashino and Prof. Hiroshi Imahori for their assistance with the HRMS measurements. We would also like to express our gratitude to the SPring-8 synchrotron facility, where synchrotron-radiation experiments were performed at the BL02B1 beamlines with the approval of the Japan Synchrotron Radiation Research Institute (JASRI) under proposal numbers 2023B1682, 2024B1931, 2024B1757, and 2024A1948.

Supporting information

Additional data are given in the supplementary material. This material is available free of charge *via* the Internet at http://www.worldscientific.com/doi/suppl/10.1142/S1088424625500397

Crystallographic data have been deposited at the Cambridge Crystallographic Data Centre (CCDC) under the numbers CCDC-2415645 and CCDC-2415646. Copies can be obtained on request, free of charge, *via* https://www.ccdc.cam.ac.uk/structures/ or from the Cambridge Crystallographic Data Centre, 12 Union Road, Cambridge CB2 1EZ, UK (fax: +44 1223-336-033 or email: deposit@ccdc.cam.ac.uk).

REFERENCES

1. Boylan DB and Calvin M. *J. Am. Chem. Soc*. 1967; **89**: 5472–5473.
2. Pia JE, Hussein BA, Skrypai V, Sarycheva O and Adler MJ. *Coord. Chem. Rev*. 2021; **449**: 214183.
3. (a) Kane KM, Lemke FR and Petersen JL. *Inorg. Chem.* 1995; **34**: 4085–4091; (b) Lorenz CR, Dewald HD and Lemke FR. *J. Electroanal. Chem.* 1996; **415**: 179–181; (c) Kane KM, Lemke FR and Petersen JL. *Inorg. Chem.* 1997; **36**: 1354–1359; (d) Kane KM, Lorenz CR, Heilman DM and Lemke FR. *Inorg. Chem.* 1998; **37**: 669–673.
4. Zheng JY, Konishi K and Aida T. *Inorg. Chem*. 1998; **37**: 2591–2594.
5. (a) Ishida S, Yoshimura K, Matsumoto H and Kyushin S. *Chem. Lett*. 2009; **38**: 362–363; (b) Ishida S, Hatakeyama T, Nomura T, Matsumoto M, Yoshimura K, Kyushin S and Iwamoto T. *Chem. Eur. J*. 2020; **26**: 15811–15815.
6. Hussein BA, Shakeel Z, Turley AT, Bismillah AN, Wolfstadt KM, Pia JE, Pilkington M, McGonigal PR and Adler MJ. *Inorg. Chem*. 2020; **59**: 13533–13541.
7. (a) Cissell JA, Vaid TP and Rheingold AL. *J. Am. Chem. Soc.* 2005; **127**: 12212–12213; (b) Cissell JA, Vaid TP and Yap GPA. *J. Am. Chem. Soc.* 2007; **129**: 7841–7847; (c) Cissell JA, Vaid TP, DiPasquale AG and Rheingold AL. *Inorg. Chem.* 2007; **46**: 7713–7715.
8. (a) Satoh T, Minoura M, Nakano H, Furukawa K and Matano Y. *Angew. Chem. Int. Ed.* 2016; **55**: 2235–2238; (b) Sudoh K, Satoh T, Amaya T, Furukawa K, Minoura M, Nakano H and Matano Y. *Chem. Eur. J.* 2017; **23**: 16364–16373; (c) Sudoh K, Satoh Y, Furukawa K, Nakano H and Matano Y. *J. Porphyrins Phthalocyanines* 2020; **24**: 286–297; (d) Satoh Y, Fujita Y, Muramatsu N, Furukawa K, Ikoma T, Minoura M, Nakano H and Matano Y. *ChemPlusChem* 2021; **86**: 1476–1486; (e) Ochiai H, Furukawa K, Nakano H and Matano Y. *J. Org. Chem.* 2021; **86**: 2283–2296; (f) Satoh Y, Kudoh Y, Furukawa K and Matano Y, *Org. Lett.* 2022; **24**: 3839–3843.
9. (a) Sudoh K, Hatakeyama T, Furukawa K, Nakano H and Matano Y. *J. Porphyrins Phthalocyanines* 2018; **22**: 542–551; (b) Murata Y, Sudoh K, Furukawa K, Nakano H and Matano Y. *Chem. Asian J.* 2024; **19**: e202401370.
10. Suzuki H, Furukawa K, Minoura M, Nakano H and Matano Y. *Bull. Chem. Soc. Jpn.* 2024; **97**: uoad022.
11. Matano Y, Shibano T, Nakano N, Kimura Y and Imahori H. *Inorg. Chem.* 2012; **51**: 12879–12890.
12. Hamilton WC. *Acta Crystallogr*. 1962; **15**: 353–360.
13. Ou X and Janzen AF. *Inorg. Chem*. 1997; **36**: 392–395.
14. McDowell RS, Reisfeld MJ, Patterson CW, Krohn BJ, Vasquez MC and Laguna GA. *J. Chem. Phys.* 1982; **77**: 4337–4343.
15. (a) Krygowski TM. *J. Chem. Inf. Comput. Sci.* 1993; **33**: 70–78; (b) Krygowski TM, Ciesielski A, Bird CW and Kotschy A, *J. Chem. Inf. Comput. Sci.* 1995; **35**: 203–210; (c) Cyrański MK, Krygowski TM, Wisiorowski M, van Eikema Hommes NJR

and Schleyer PvR. *Angew. Chem. Int. Ed.* 1998; **37**: 177–180.

16. Matano Y, Shibano T, Nakano H and Imahori H. *Chem. Eur. J.* 2012; **18**: 6208–6216.
17. (a) Schleyer PvR, Maerker C, Dransfeld A, Jiao H and van Eikema Hommes NJR. *J. Am. Chem. Soc.* 1996; **118**: 6317–6318; (b) Chen Z, Wannere CS, Corminboeuf C, Puchta R and Schleyer PvR. *Chem. Rev.* 2005; **105**: 3842–3888.
18. The ^{19}F chemical shift of **P1** (18π) is −114.1 ppm (vs. $CFCl_3$). See ref. 10.
19. (a) Krishnan R, Binkley JS, Seeger R and Pople JA. *J. Chem. Phys.* 1980; **72**: 650–654; (b) McLean AD and Chandler GS. *J. Chem. Phys.* 1980; **72**: 5639–5648; (c) Francl MM, Pietro WJ, Hehre WJ, Binkley JS, Gordon MS, DeFrees DJ and Pople JA. *J. Chem. Phys.* 1982; **77**: 3654–3665.
20. (a) Becke AD. *J. Chem. Phys.* 1993; **98**: 5648–5652; (b) Lee C, Yang W and Parr RG. *Phys. Rev. B* 1988; **37**: 785–789.
21. Cancès E, Mennucci B and Tomasi J. *J. Chem. Phys.* 1997; **107**: 3032–3041.
22. (a) Hehre WJ, Ditchfield R and Pople JA. *J. Chem. Phys.* 1972; **56**: 2257–2261; (b) Hariharan PC and Pople JA. *Theor. Chim. Acta* 1973; **28**: 213–222; (c) Clark T, Chandrasekhar J, Spitznagel GW and Schleyer PvR. *J. Comput. Chem.* 1983; **4**: 294–301; (d) Gordon MS, Binkley JS, Pople JA, Pietro WJ and Hehre WJ. *J. Am. Chem. Soc.* 1982; **104**: 2797–2803; (e) Spitznagel GW, Clark T, Schleyer PvR and Hehre WJ. *J. Comput. Chem.* 1987; **8**: 1109–1116.
23. Frisch MJ, Trucks GW, Schlegel HB, Scuseria GE, Robb MA, Cheeseman JR, Scalmani G, Barone V, Petersson GA, Nakatsuji H, Li X, Caricato M, Marenich AV, Bloino J, Janesko BG, Gomperts R, Mennucci B, Hratchian HP, Ortiz JV, Izmaylov AF, Sonnenberg JL, Williams-Young D, Ding F, Lipparini F, Egidi F, Goings J, Peng B, Petrone A, Henderson T, Ranasinghe D, Zakrzewski VG, Gao J, Rega N, Zheng G, Liang W, Hada M, Ehara M, Toyota K, Fukuda R, Hasegawa J, Ishida M, Nakajima T, Honda Y, Kitao O, Nakai H, Vreven T, Throssell K, Montgomery JA Jr, Peralta JE, Ogliaro F, Bearpark MJ, Heyd JJ, Brothers EN, Kudin KN, Staroverov VN, Keith TA, Kobayashi R, Normand J, Raghavachari K, Rendell AP, Burant JC, Iyengar SS, Tomasi J, Cossi M, Millam JM, Klene M, Adamo C, Cammi R, Ochterski JW, Martin RL, Morokuma K, Farkas O, Foresman JB and Fox DJ. *Gaussian 16*, Revision C.01, Gaussian, Inc., Wallingford CT, 2019.
24. Stoll S and Schweiger A. *J. Magn. Reson*. 2006; **178**: 42–55.